Nanoscale Advances

ROYAL SOCIETY OF CHEMISTRY

REVIEW

View Article Online
View Journal | View Issue

Cite this: *Nanoscale Adv.*, 2020, **2**, 4986

The role of oxygen defects in metal oxides for CO_2 reduction

Zesheng Deng,† Jiahui Ji,† Mingyang Xing * and Jinlong Zhang *

The abuse of fossil fuels release large amount of CO_2, causing intense global warming. Using photoreduction and electroreduction to convert CO_2 into highly valuable fuels such as CO and CH_4 can effectively solve this problem. However, due to the limited activity and selectivity, pristine catalyst materials cannot meet the requirements of practical applications, which means that some modifications to these catalysts are necessary. In this review, a series of research reports on oxygen defect engineering have been introduced. First, the methods of preparing oxygen defects by heat treatment, doping, and photoinduction combined with influencing factors in the preparation are introduced. Subsequently, common characterization methods of oxygen defects including EPR, Raman, XPS, EXAFS, and HRTEM are summarized. Finally, the mechanisms of introducing oxygen defects to improve CO_2 reduction are discussed, and include enhancing light absorption, improving CO_2 adsorption and activation, as well as promoting stability of the reaction intermediates. The summary of research on oxygen defects provides guidance for researchers who focus on CO_2 reduction and accelerate the realization of its industrial applications in the future.

Received 28th June 2020
Accepted 22nd August 2020

DOI: 10.1039/d0na00535e

rsc.li/nanoscale-advances

1. Introduction

1.1 Background

For decades, the consumption of fossil fuels has caused a sharp rise in the level of CO_2 emission, and has resulted in some serious problems related to global warming and climate change.[1,2] Therefore, it is necessary to take some measures to limit and reduce CO_2 emission. The capture and conversion of CO_2 into reusable value-added chemicals is considered an effective method to remove excess CO_2 from air.[3,4] Therefore, the photoreduction and electroreduction of CO_2 are considered to be environment-friendly methods for converting CO_2 into combustible chemicals (such as CO and CH_4), followed by the development of a large number of photocatalysts and electrocatalysts.[5–8] The defects contained in the catalysts play an important role in capturing CO_2 and lowering the activation energy of adsorbed CO_2.[9–11] In this review, various materials with oxygen defects have been discussed to gain more insight into the correlation between oxygen defects and the activity and selectivity of CO_2 photoreduction and electroreduction. Finally,

Key Laboratory for Advanced Materials and Joint International Research Laboratory of Precision Chemistry and Molecular Engineering, Feringa Nobel Prize Scientist Joint Research Center, School of Chemistry and Molecular Engineering, East China University of Science and Technology, 130 Meilong Road, Shanghai 200237, China. E-mail: mingyangxing@ecust.edu.cn; jlzhang@ecust.edu.cn

† Zesheng Deng and Jiahui Ji contributed equally to this work.

Zesheng Deng is a PhD student at East China University of Science and Technology (ECUST, Shanghai, China). He obtained his bachelor's degree from ECUST, then joined Prof. Jinlong Zhang's group in 2018. His research interest focuses on CO_2 photoreduction.

Jiahui Ji is PhD student at East China University of Science and Technology (ECUST, Shanghai, China). He obtained his bachelor's degree from Nanjing Tech University, then joined Prof. Mingyang Xing's group in 2017. His research interest focuses on Advanced Oxidation Technologies (AOTs) such as photocatalysis and Fenton reactions.

the role of oxygen defect-rich catalysts in the conversion of CO_2 to reusable fuel is summarized and their future applications are investigated.

1.2 Mechanisms of CO_2 photoreduction and electroreduction

Photoreduction and electroreduction processes have been proved to be effective methods for the removal of excessive CO_2 in air.[12–14] Moreover, there are some differences in the mechanisms between CO_2 electroreduction and photoreduction.

Since the pioneering work on photoelectrochemical water splitting that was reported by Fujishima and Honda in 1972,[15] CO_2 photoreduction has gradually developed and studied extensively. As shown in Fig. 1A, the generally accepted process of CO_2 photoreduction is as follows: first, the photoexcited electrons are excited from the valence band to the conduction band, leaving holes in the valence band. Then, the electrons and holes are separated, which migrate to the surface of the catalysts to reduce CO_2 to combustible chemicals (such as CO and CH_4).[16] The valence state of carbon in CO_2 is the highest oxidation state; thus, there are various reduction products of CO_2, ranging from CO and CH_4 to higher hydrocarbons and oxygenates such as CH_3OH and HCOOH. On the other hand, the actual process of CO_2 photoreduction is slightly complicated. Consider the case of CO as the only photocatalytic product. As eqn (1)–(5) show, first, the photogenerated electrons combine with CO_2 and H^+ to form the intermediate *COOH. Then, *COOH combines with the photogenerated electrons and H^+ to release H_2O and to obtain CO absorbed on the catalyst's surface. Finally, CO is desorbed from the catalyst surface. In the meantime, photogenerated holes combine with water to produce oxygen and H^+. Due to the complex process of CO_2 reduction, there are many factors that influence the activity and selectivity of CO_2 photoreduction. Solar light harvesting, charge separation and transportation, as well as surface reactions, are the three main factors, which is recognized as crucial for improving the selectivity and activity of CO_2 photoreduction. In fact, it is difficult for the pristine catalyst to meet all requirements. While, introducing oxygen defects is an effective method to solve these problems.

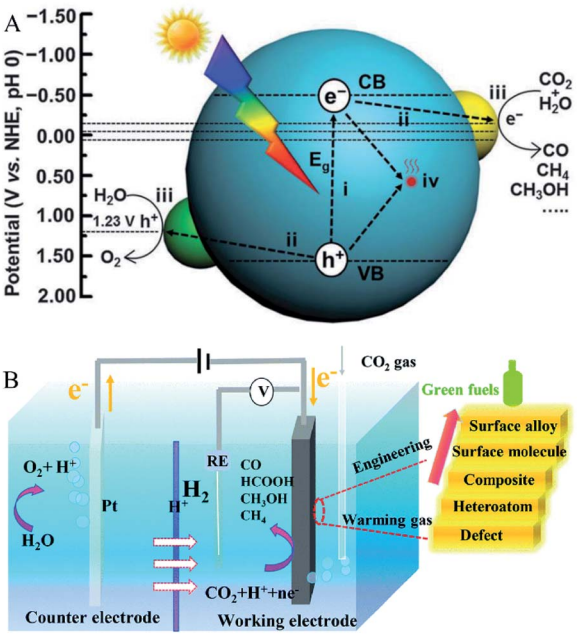

Fig. 1 (A) Schematic illustration of CO_2 photoreduction. Reproduced with permission: Copyright The Royal Society of Chemistry 2016;[16] (B) schematic illustration of CO_2 electroreduction. Reproduced with permission: Copyright The Royal Society of Chemistry 2019.[17]

Dr Mingyang Xing is a Professor and supervisor of postgraduate students at the School of Chemistry and Molecular Engineering, East China University of Science and Technology (ECUST). He obtained his doctoral degree in 2012 from ECUST and then worked at University of California, Riverside, as a visiting scholar for one year. His research focuses on the design and preparation of functional nanomaterials and applications to the environment and energy fields. He has published more than 90 papers in SCI journals in these areas, which have been cited more than 6800 times (H-index: 46).

Prof. Dr Jinlong Zhang obtained his bachelor's degree in 1985 and his PhD in 1993 from East China University of Science and Technology, Shanghai, China. Professor Zhang joined the East China University of Science and Technology in 1993. He worked at Osaka Prefecture University as a Postdoctoral candidate (JSPS) while collaborating with Prof. Anpo from 1996 to 2000. He became a full professor in 2000. He has published over 350 original papers, which were cited more than 22 000 times (H-index: 76). He is currently on the editorial boards of "Applied Catalysis B: Environmental" and "Scientific Reports". He is also the associate editor of "Res. Chem. Intermed.". His research interests include photocatalysis, mesoporous materials, and materials science. He has been selected as one of the "Most Cited Chinese Researchers" in China by "Elsevier" in 2014, 2015, 2016, 2017, and 2018.

$$CO_2 + e^- + * + H^+ \rightarrow *COOH \quad (1)$$

$$*COOH + e^- + H^+ \rightarrow *CO + H_2O \quad (2)$$

$$*CO \rightarrow CO + * \quad (3)$$

$$2H_2O + 4h^+ \rightarrow O_2 + 4H^+ \quad (4)$$

$$2H^+ + 2e^- \rightarrow H_2 \quad (5)$$

As for the electric reduction process of CO_2, it mainly relies on the electrons generated in the electrode to reduce the CO_2 adsorbed on the electrocatalyst electrode. As shown in Fig. 1B, electrocatalytic CO_2 reduction usually occurs in a three-electrode system, including a working electrode loaded with the electrocatalyst for CO_2 reduction, a reference electrode for determining the potential, and a counter electrode that balances the charge and the current. In the process of CO_2 electroreduction, electrons transfer to the working electrode and reduce the adsorbed CO_2 to valuable fuels such as HCOOH and CO.[17] There are many factors that affect CO_2 electroreduction, such as the applied potential, the nature of the electrolyte solution, and the electrocatalyst. In this review, the roles of oxygen-defect electrocatalysts applied in CO_2 electroreduction are mainly discussed. As published in the literature, the process for converting CO_2 to CO involves the steps shown in eqn (6)–(8) and the process of hydrogen evolution involves the steps shown in eqn (9) and (10).[18–20] At the beginning of the reaction, CO_2 is adsorbed on the electrocatalyst first and then reduced to the intermediate *COOH, which is further transformed to H_2O and CO, and then desorbed from the electrocatalysts. When the electrocatalyst has the best CO binding energy, it can promote further reaction with other reduction products, such as CH_4 and CH_3OH. As reported in the literature, the two main limitations of CO_2 electroreduction activity are *COOH formation and hydrogen evolution.

$$CO_2(g) + e^- + * + H^+ \rightarrow *COOH \quad (6)$$

$$*COOH + e^- + * + H^+ \rightarrow *CO + H_2O(l) \quad (7)$$

$$*CO \rightarrow CO(g) + * \quad (8)$$

$$H^+ + e^- + * \rightarrow *H \quad (9)$$

$$*H + H^+ + e^- \rightarrow * + H_2 \quad (10)$$

1.3 The role of oxygen defects

Among the strategies for improving catalytic CO_2 reduction, introducing oxygen defects into the catalysts has become one of the most likely ways to achieve this goal. The introduction of oxygen defects can enhance the conductivity of the catalysts, and generate a large number of activation sites and adsorption sites on these catalysts, which help to improve their ability for CO_2 reduction. A large number of studies have reported that oxygen defect-rich catalysts play a very effective role in CO_2 reduction.[11,21–24] The formation of oxygen defects can modify the optical absorption by introducing a defective level in order to reduce the bandgap, which further enhances the activity of the catalysts in CO_2 reduction. Moreover, the formation of the oxygen defects is usually accompanied by the exposure of the metal cation of the metal oxide catalysts and surface atomic structure modification of the catalysts, which may expose more active sites on the catalysts, thus leading to the enhancement in the adsorption and activation of CO_2 in CO_2 reduction.[25] According to the studies, the oxygen defects exposed on the surface of the catalysts can offer chemical adsorption sites to reduce the CO_2 adsorption energy, activate CO_2 by bending or stretching the C=O bond, and lower the energy barrier by stabilizing the intermediates. It can be anticipated that the introduction of oxygen defects can really improve the CO_2 reduction efficiency.

Therefore, in order to further intuitively understand the role of oxygen defects in CO_2 reduction and the corresponding mechanism, we have summarized the different preparation methods of oxygen defect-rich catalysts, the characterization of oxygen defects, and the mechanism involving promotion of CO_2 reduction by the introduction of oxygen defects.

2. The introduction of oxygen defects

Oxygen defect engineering has been widely utilized to adjust the electronic structure of the target catalysts and to improve their performance in CO_2 reduction. According to the published reports, oxygen defects are usually introduced by methods such as heat treatment, irradiation, or doping modification.

2.1 Introducing oxygen defects by heat treatment

Oxygen defects are created by removing oxygen atoms from the catalyst. The common methods for removing oxygen atoms include using a strong reducing agent to reduce the catalyst, reducing the ambient oxygen partial pressure (such as anaerobic condition), and introducing interfacial lattice strain to reduce the Gibbs free energy of oxygen defect formation, so that the reaction balance can move toward the direction of oxygen defects' generation.

There are many methods of introducing oxygen defects through thermal induction operated in vacuum or inert gas environment.[26–28] Wang *et al.*[29] reported a strategy to control the oxygen defect concentration by annealing ZnO nanoparticles in different atmospheres with different oxygen partial pressures at 550 °C for 2 h. By comparing the oxygen defect concentration of the ZnO samples annealed in oxygen, air, and nitrogen atmospheres, it was found that the order of oxygen defect concentration on the surface of the ZnO samples was nitrogen > air > oxygen annealing environments. This result was consistent with the assumption that a lower oxygen defect concentration was obtained in a higher oxygen partial pressure during the heat treatment, demonstrating that the oxygen partial pressure during the heat treatment did have a great effect on the oxygen defect concentration.

In addition to decreasing the partial pressure of oxygen, studies have shown that interfacial lattice strain is another important factor that controls the generation of oxygen defects. Wang *et al.*[30] reported a method for introducing oxygen defects under mild heating conditions by introducing interfacial lattice strain. In this case, as shown in Fig. 2A, interfacial lattice strain was introduced in TiO_2(B) by coating transition metal oxides. The results showed that TiO_2(B) with coated transition metal oxides had a much higher ratio of oxygen defects than that with uncoated transition metal oxides. As shown in Fig. 2B, it could be calculated that the potential barrier gradually decreased as the interface lattice strain increased. The Gibbs free energy (ΔG) of oxygen defect formation could be defined as a function of epitaxial strain (η) and temperature (T), according to the following relationship, which confirmed the mechanism that the interfacial strain affected the energy barrier of oxygen defect generation (eqn (11)):

$$\Delta G = \Delta E(\eta) + \Delta F(\eta, T) + 0.5 \times \mu_0(T) \quad (11)$$

where μ_0 is the oxygen chemical potential, ΔE represents the free energy at zero temperature, and ΔF represents the thermal contribution to free energy. According to the equilibrium, the increase in the interfacial lattice strain led to the decrease in ΔG. Therefore, it could be concluded that the interfacial lattice strain introduced by coating made the oxygen defect generation thermodynamically favorable.

The temperature is another significant influencing factor of oxygen defects. According to eqn (11), temperature has a great influence on the Gibbs free energy of oxygen defect formation. The temperature determines whether the oxygen defects can be generated or not. Liu *et al.*[31] reported a method of controlling the concentration of oxygen vacancies (OVs) by annealing TiO_2 powder in hydrogen gas at different temperatures ranging from 120 °C to 700 °C. In this case, the result of the thermal treatment demonstrated that the content of oxygen defect increased at first and then decreased with the continuous increase in the annealing temperature. The whole process could be divided into three steps: firstly, hydrogen was physically adsorbed on the surface of TiO_2 below 300 °C; secondly, when the temperature was higher than 300 °C, the electrons were transferred from the hydrogen atoms to the oxygen atoms, and then the oxygen atoms were removed by the hydrogen atoms in the form of water, leaving oxygen defects on TiO_2. As a result, the oxygen defect content increased with the temperature increasing from 300 °C to 450 °C. Thirdly, when the temperature rose up to 450 °C, the electrons were transferred from the oxygen defects to Ti^{4+}, and Ti^{3+} was formed at the same time, leading to a decrease in the oxygen defects content as the temperature increased over 450 °C. The result of temperature control on the oxygen defect content showed that the OVs formation was determined by thermodynamic control. This means that the oxygen defect content increase for thermodynamically favorable processes and decrease for thermodynamically unfavorable processes.

In addition to introducing oxygen defects under the gas–solid condition by means of heating at high temperature, using a strong reducing agent in the liquid–solid condition can also effectively introduce oxygen defects at a mild temperature. Kim *et al.*[32] reported a strategy for the preparation of $BaSnO_{3-x}$ with abundant oxygen defects under the solid–liquid condition at room temperature with $NaBH_4$ as the reducing agent. In this case, they could effectively adjust the concentration of oxygen defects by controlling the amount of $NaBH_4$. Compared with the other methods for introducing oxygen defects at high temperature, this mild liquid–solid method could produce oxygen defects without high-temperature processing, which prevented the high temperature from destroying the material structure of the catalysts.

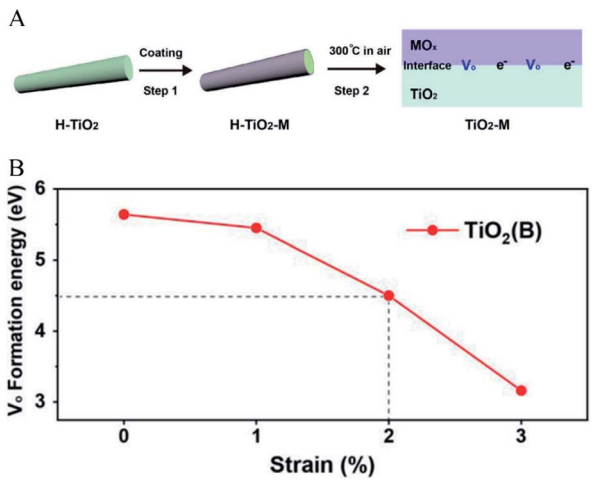

Fig. 2 (A) Illustration of the introduction of interfacial lattice strain by coating transition metal oxides, (B) the relationship between interfacial strain and oxygen defect formation energy. Reproduced with permission: Copyright 2019 Wiley-VCH Verlag GmbH & Co. KGaA, Weinheim.[30]

2.2 Introducing oxygen defects by doping

The traditional method of generating oxygen defects is heat treatment at a high temperature, which has some problems in keeping the structure and morphology unchanged. The method of introducing oxygen defects by doping heteroatoms is feasible for triggering oxygen defects in order to maintain the stability even under oxygen-rich circumstances. Liu *et al.*[33] reported a facile strategy for introducing oxygen defects by annealing commercial MO_3 at 300 °C in a NH_3 atmosphere. The N-doped MO_3 obtained from the heat treatment had advantages in attaining stable oxygen defects by decreasing the formation energy of the oxygen defects. Zhang *et al.*[34] reported another method of doping boron atom into transition metal oxides to form stable oxygen defects by the pyrolysis approach. The result indicated that boron doping reduced the generation energy of oxygen defect formation in transition metal oxides, which made the generation of oxygen defects thermodynamically favorable. Moreover, substituting the transition metal with the doping cation is also an effective way to introduce oxygen defects. Zhao *et al.*[35] reported a method for precisely controlling the concentration of the oxygen defects by Cu doping under the

hydrothermal condition. Cu/TiO_2 was synthesized with different amounts of Cu ions, which determined the concentration of the oxygen defects. It was proved that the Ti–O coordination number was decreased as the amount of the doping Cu ions increased, which made it easy for to release oxygen and thereby increase the oxygen defect content. These evidences demonstrate that the concentration of oxygen defects could be controlled by cation substitution. Tong *et al.*[25] also reported an Fe-doping method for the introduction of oxygen defects in WO_{3-x}. Fe-doped WO_{3-x} was prepared by the hydrothermal method in ethanol solvent, with $FeCl_3$ and WCl_6 used as the precursors. In this case, with the increase in the amount of doped iron, the oxygen defect concentration increased gradually. The low valence state cation substituted the high valence state cation, which would reduce M–O (M is the metal cation) bond and release oxygen; thus, with the increase in cation-doping, the oxygen defect concentration increased gradually. Usually, the activity of the catalysts has an optimal point; thus, that the cation-doping method could control the oxygen defect concentration for obtaining the optimal activity.

2.3 Introducing oxygen defects by illumination

The creation of oxygen defects by photoinduction is a facile method. As for the metal oxide semiconductors, the photoelectrons can be excited by illumination and transferred from oxygen to metal cation, then the oxygen atoms are released and simultaneously form the oxygen defects. Feng *et al.*[36] reported a method for introducing oxygen defects by illumination. The whole process of generating oxygen defects was operated at room temperature by the photoetching method. As shown in Fig. 3, $BiVO_4$ with abundant oxygen defects was obtained by immersing the $BiVO_4$ photoanode into the electrolyte containing alkali solution and sodium sulfate with illumination. This photoetching method increased the donor density without introducing a heteroatom and maintained the structure of the $BiVO_4$ photoanode. Therefore, the method offered a facile modification strategy to attain oxygen defects. Ye and co-workers[37] have reported a photoinduced oxygen defect engineering method to fabricate black In_2O_{3-x} nanosheets. They adopted a 300 W Xe lamp as the irradiation source and introduced oxygen defects in an H_2/CO atmosphere. During the process of introducing oxygen defects, h^+ was reduced by CO or H_2 and the photogenerated electron reduced In_2O_3 to In_2O_{3-x} so as to introduce oxygen defects. Zhang *et al.*[38] have reported a method of introducing oxygen defects in BiOCl by illumination. BiOCl was irradiated under a 500 W Xe lamp for 5 h, then the white BiOCl turned to gray defective BiOCl. The introduction of oxygen defects can be effectively controlled by the illumination method. These obtained oxygen defects can effectively widen the photoabsorption range of the catalysts, and improve the CO_2 adsorption and the catalytic activity. The photoinduction method is an ideal strategy to regenerate oxygen defects in catalysts without introducing a heteroatom and breaking the structure of the catalysts.

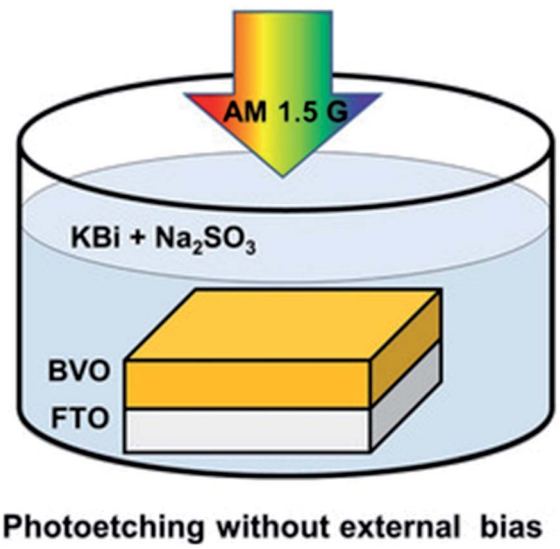

Fig. 3 Illustration of the introduction of oxygen defects by photoetching. Reproduced with permission: Copyright 2020 Wiley-VCH Verlag GmbH & Co. KGaA, Weinheim.[36]

3. Characterization of the oxygen defects

In the process of studying the role of defective catalysts in CO_2 reduction, it is usually required to characterize the type and quantity of defects introduced into the catalysts, including the oxygen defects. Common defects characterization methods include high resolution transmission electron microscopy (HRTEM), X-ray photoelectron spectroscopy (XPS), Raman spectroscopy, electron paramagnetic resonance (EPR), X-ray absorption fine structure (XAFS), and photoluminescence (PL); it is usually necessary to combine some of these methods for defect characterization.

Liu *et al.*[39] synthesized OVs-enriched blue WO_{3-x} porous nanorods (OBWPN) without N-doping by a simple method. Fig. 4A is the HRTEM image of OBWPN, in which the lattice fringe of 0.375 nm is clearly observed, indexed to the (020) plane of WO_3. The amorphous areas of OBWPN marked with a yellow circle proved that its crystallinity had decreased. Comparing the XRD spectra of yellow WO_3 porous nanorods (YWPN) and OBWPN (Fig. 4B), the two XRD patterns are similar but the peak intensity of OBWPN is relatively weak, further proving that its crystallinity was reduced, which was attributed to the formation of OVs. XPS was employed to confirm the formation of OVs as well. As shown in the O 1s XPS spectra (Fig. 4C), both YWPN and OBWPN contain two typical peaks at 530.3 and 532.6 eV, which represent the W–O bonds and the hydroxyl species of water molecules adsorbed on the surface, respectively. Moreover, the unique peak of OBWPN at 531.2 eV indicates the existence of OVs, proving that the ammonia-assisted reduction strategy introduced OVs in OBWPN. In order to search for more evidences for the existence of OVs, XAFS at W L3-edge and PL spectroscopy were carried out. Fig. 4D is the X-ray absorption near-edge structure (XANES) of YWPN and OBWPN. Compared with YWPN, the peak of OBWPN decreased significantly,

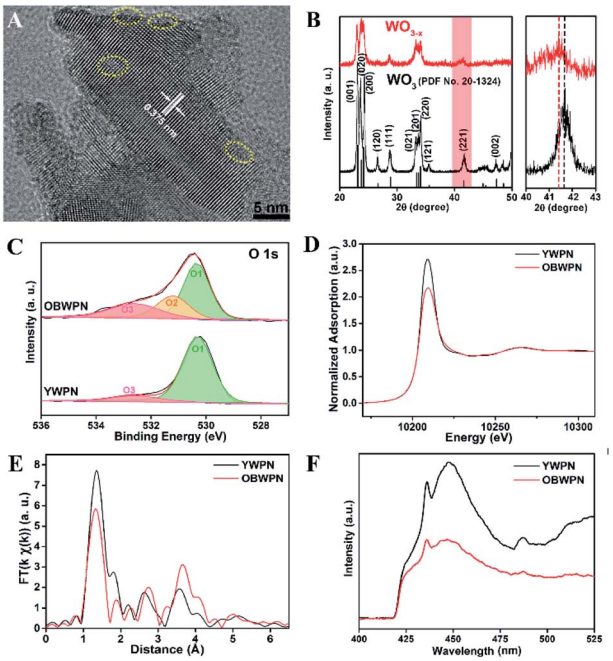

Fig. 4 (A) HRTEM image of OBWPN, (B) XRD patterns of YWPN (black) and OBWPN (red), (C) O 1s XPS spectra of YWPN and OBWPN, (D) normalized W L_3-edge XANES spectra of YWPN and OBWPN, (E) fourier transform (FT) of k-weighted W EXAFS spectra of YWPN and OBWPN, (F) photoluminescence spectra of YWPN and OBWPN. Reproduced with permission: Copyright 2018 Elsevier Inc.[39]

indicating that OVs caused the decrease in the W valence of OBWPN. Fig. 4E exhibits the fourier transform (FT) of k-weighted W EXAFS spectra for YWPN and OBWPN. The peak at ~1.33 Å represents the W–O bond. The W–O peak magnitude of OBWPN was lower than that of YWPN, indicating that the formation of OVs reduced the W–O coordination number in OBWPN. Comparing the fluorescence peaks at 440 nm in the PL spectra of YWPN and OBWPN (Fig. 4F), it can be observed that the peak of OBWPN is weaker, which means that its recombination rate of photogenerated electrons and holes is lower, caused by OVs.

Ahmed *et al.*[40] has synthesized TG (TiO_2 modified by reduced graphene oxide) to reduce the ratio of the relative concentration of the bulk defects to the surface defects so as to improve CO_2 photoreduction. PALS (positron annihilation lifetime spectroscopy) was employed to quantify the relative concentrations of these defects. As observed from Table 1, three positron lifetime components τ_1, τ_2, τ_3 and their relative intensities I_1, I_2, I_3 were recorded. The positron lifetimes τ_1, τ_2, and τ_3 are attributed to the bulk defects, surface defects, and micropores as well as the annihilation of orthopositronium atoms, respectively. In addition, I_1, I_2, I_3 are the relative intensity of τ_1, τ_2, τ_3, and the ratio of I_1/I_2 is assigned to the relative defect concentration of the bulk to the surface. In this case, the TG had a lower ratio of I_1/I_2, which indicated that the coupling of graphene reduced the relative concentration of the bulk defects to the surface defects. Considering that TG has a much higher CO_2 reduction activity, this result effectively proved that the surface oxygen defects can improve the photocatalytic activity more effectively.

Table 1 Positron lifetime and relative intensities of TiO_2 and TG.[40] Reproduced with permission: Copyright 2019, Springer Nature

Sample	τ_1 (ns)	τ_2 (ns)	τ_3 (ns)	I_1 (%)	I_2 (%)	I_3 (%)	I_1/I_2
TiO_2	0.1985	0.3937	2.2900	54.4	43.9	1.76	1.23
TG	0.2069	0.3864	2.3130	50.1	48.3	0.67	1.03

Karmakar *et al.*[41] explored the role of OVs in enhancing the photoelectrochemical properties of alkali metal (Li, Na, and K) doped ZnO nanorods. The doped alkali metal ions replaced the zinc ions, leaving extra holes, which required electrons to neutralize, thus forming the OVs simultaneously. Through XPS analysis, it could be found that the O 1s spectra of the alkali metal doped ZnO NRs had broad peaks and could be divided into two peaks located at 531.6 eV and 529.9 eV, which represented OVs and O^{2-} ions, respectively. The peak intensity of the OVs was related to their concentration. As shown in Fig. 5A, the peak intensities of OVs of Li and Na–ZnO NRs were higher than that of K–ZnO NRs. In this order, the corresponding peak area ratios of their OVs were 0.85, 0.83, and 0.67, respectively, which demonstrated that Li and Na–ZnO NRs contained almost equal OVs concentrations, more than that of the K–ZnO NRs (Fig. 5B). The room temperature PL emission spectra display that the doped ZnO NRs showed significant sub-band gap defect emission near 490 nm, as shown in Fig. 5C, and this deep level emission (DLE) is usually attributed to oxygen-vacancy defects.

In order to enhance the efficiency of photocatalytic CO_2 reduction, Wu *et al.*[42] used high-energy ultraviolet irradiation to produce a large number of OVs on the (001) surface of BiOBr, and characterized the existence of OVs by means of XPS, XAFS, EPR, *etc.* As shown in Fig. 6A, UV-vis diffuse reflectance spectroscopy was used to confirm the existence of OVs in the BiOBr atomic layer. With the increase in the ultraviolet radiation to the BiOBr atomic layer, a gradually increasing new absorption peak appeared in the visible region, which was due to the formation of OVs. The absorption of visible light by the BiOBr atomic layer reached its maximum value when irradiated with ultraviolet

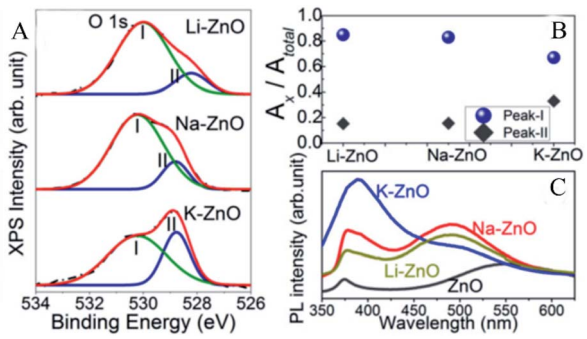

Fig. 5 High-resolution XPS spectra of (A) O 1s for the doped ZnO NRs, (B) the peak area ratios of peak-I and peak-II to the total area, (C) room-temperature PL emission spectra of the alkali metal doped ZnO NRs. Reproduced with permission: Copyright 2018 Wiley-VCH Verlag GmbH & Co. KGaA, Weinheim.[41]

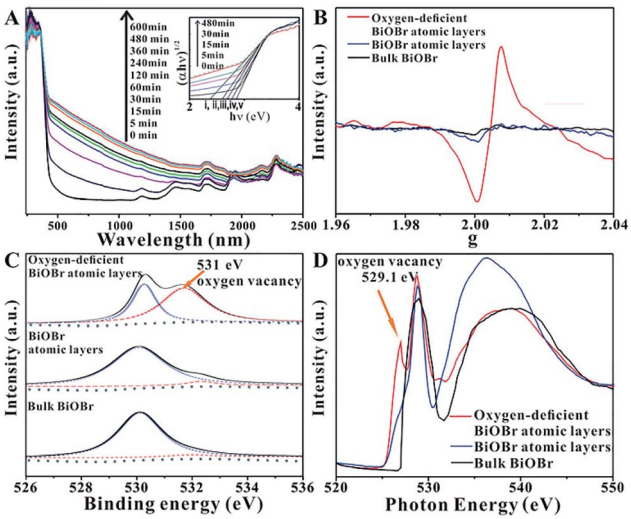

Fig. 6 (A) UV-vis diffuse reflectance spectra for the BiOBr atomic layers after UV irradiation for different periods of time, (B) EPR spectra, (C) high-resolution O 1s XPS spectra, (D) O K-edge XANES spectra for oxygen-deficient BiOBr atomic layers, BiOBr atomic layers, and bulk BiOBr (oxygen-deficient BiOBr atomic layers represent BiOBr atomic layers after UV irradiation for 480 min). Reproduced with permission: Copyright 2018 Wiley-VCH Verlag GmbH & Co. KGaA, Weinheim.[42]

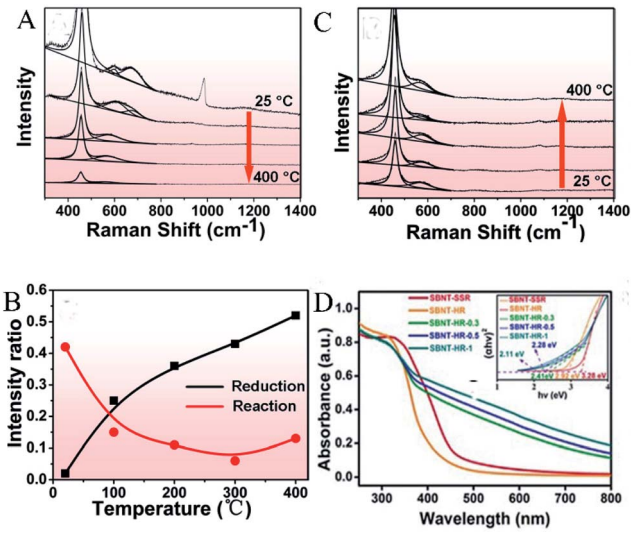

Fig. 7 Operando visible Raman spectra of the Ru/CeO_2 catalyst in (A) the reduction process, (B) the reaction process. The temperature points selected in each process: 25, 100, 200, 300, and 400 °C. (C) The corresponding $I_D/I_{F_{2g}}$ value as a function of temperature in the reduction and reaction process. Reproduced with permission: Copyright 2020 American Chemical Society.[43] (D) UV-vis diffuse reflectance spectra (DRS), band gap (inset). Reproduced with permission: Copyright 2019 Wiley-VCH Verlag GmbH & Co. KGaA, Weinheim.[44]

light for 480 minutes, indicating that the oxygen defect concentration reached its maximum value at this time. In response to this situation, EPR technology was used to further prove the existence of the OVs. Fig. 6B shows that the bulk BiOBr and BiOBr atomic layers have no obvious EPR signal, indicating that there are almost no OVs. In contrast, the BiOBr atomic layer, after ultraviolet irradiation for 480 min, showed the strongest EPR signal at $g = 2.004$, indicating that ultraviolet irradiation did indeed cause OVs in the BiOBr atomic layer. As observed from Fig. 6C, the high-resolution O 1s XPS spectrum shows that after 480 min of ultraviolet irradiation, a new peak at 531.4 eV appears, which is a peak formed by the oxygen atoms near the OVs. In addition, as shown in Fig. 6D, the same conclusion can be obtained from the O K-edge XANES spectra. The extra peak centered at 529.1 eV can be attributed to the OVs caused by ultraviolet light irradiation.

In order to understand the active site-dependent reaction mechanism, Wang *et al.*[43] used operando spectroscopy methodology to study the Ru/CeO_2 catalytic CO_2 methanation reaction. OVs usually play an important role in the dissociation of oxidative bonds. Therefore, operando Raman was used to detect the changes in the OVs concentration in CeO_2 during the reaction. As shown in Fig. 7A and B, the relative peak intensity ratio between the defect-induced (D) mode peak (~570 cm^{-1}) and the first-order F_{2g} peak (~460 cm^{-1}) is related to the OV concentration in CeO_2, and Fig. 7C records the value of $I_D/I_{F_{2g}}$. During the reduction, as the temperature increased from 25 °C to 400 °C, the value of $I_D/I_{F_{2g}}$ increased from 0.02 to 0.52, proving that OVs were gradually generated during the catalyst reduction process. However, when the reaction gases (CO_2 and H_2) participated, the intensity ratio dropped sharply from 0.43 (at 25 °C) to 0.15 (at 100 °C), and remained low in the temperature range of 200–400 °C.

4. Mechanism of oxygen-defects improving the CO_2 reduction

Due to poor light absorption, slow charge separation, and inefficient surface-active sites, developing effective catalysts for achieving the conversion of CO_2 into useful fuels faces enormous challenges. In recent years, the introduction of oxygen defects has become one of the most effective ways to improve the catalytic efficiency of catalysts.

4.1 Increasing the optical absorption

The light absorption capacity of a photocatalyst determines its efficiency of using solar energy. Yu *et al.*[44] reported a simple and controllable *in situ* reduction method for the introduction of oxygen defects on the surface of Aurivillius-phase $Sr_2Bi_2Nb_2TiO_{12}$ (SBNT-HR). By the *in situ* treatment of SBNT-HR with 0.3, 0.5, and 1 mL glyoxal, various OVs-rich $Sr_2Bi_2Nb_2TiO_{12}$ (SBNT-HR-X, $X = 0.3, 0.5, 1$) were obtained. As shown in Fig. 7D, the light absorption range of SBNT-HR-X extended to 800 nm and as the amount of glyoxal used increased, its light absorption capacity also gradually increased, which might be caused by the increase in the oxygen defect concentration. SBNT-HR (absorption edge of 420 nm) and bulk WO_3 obtained by the high-temperature solid–state reaction (SBNT-SSR, absorption edge of 460 nm) are relatively weak in the visible region. The inset in Fig. 7D shows that the band gaps of SBNT-SSR, SBNT-HR, and SBNT-HR-X ($X = 0.3, 0.5, 1$) are 3.28, 2.92, 2.41, 2.28, and 2.11 eV, respectively. This is because the introduced OVs brings a new defect level to the band gap, thus extending the excitation light range to the entire visible light region.

Similarly, in order to enhance the absorption of visible light, Hou *et al.*[45] prepared sodium tantalate nanocubes with nitrogen and oxygen-vacancy confined (OVs-NaTaON) for efficient photocatalytic CO_2 reduction. Fig. 8A shows the optical absorption of $NaTaO_3$ and OVs-NaTaON crystals through UV-vis diffuse reflection spectroscopy. The absorption edge of original $NaTaO_3$ is about 315 nm and its band gap is 3.78 eV (Fig. 8B), while the visible light absorption wavelength range of the OVs-NaTaON nanocrystals is up to 600 nm, corresponding to the band gap of 2.18 eV, as shown in the plots of the transformed Kubelka–Munk function *vs.* the light energy. The greatly reduced band gap proved that the introduction of OVs significantly improved the ability of the catalyst to absorb visible light. The illustration in Fig. 8B shows that the macro color of the catalyst changed from white to orange, which more clearly showed its enhanced visible light absorption capacity.

4.2 Increasing the active sites and enhancing CO_2 adsorption

The CO_2 reduction processes includes four steps: adsorption, activation, reaction, and desorption. The introduction of oxygen defects can not only contribute to the enrichment of CO_2 on the catalyst surface but can also serve as an electron capture center to reduce the recombination of electrons and holes as well as to provide more CO_2 activation sites.

Gao *et al.*[46] used the synthesized single-unit-cell layers of anoxic cobalt oxide as an example to construct a model for confining OVs in the atomic layer. As shown in the results of linear sweep voltammetry (LSV) in Fig. 9A, the large cathodic peaks at *ca.* −0.87 V *versus* saturated calomel electrode (SCE) could be ascribed to CO_2 reduction, where the current density of the OVs-rich Co_3O_4 single-unit-cell layers was approximately twice that of the OVs-poor Co_3O_4 single-unit-cell layers, indicating that the introduction of OVs was able to improve the ability of catalytic CO_2 reduction. Fig. 9B shows the result that the maximum faradaic efficiency of the OVs-rich and OVs-poor Co_3O_4 single-unit-cell layers was 87.6% and 67.3% for the production of formate at the potential of −0.87 V *versus* SCE, respectively, further proving the superior selectivity of the former in formate production. The improvement in CO_2 reduction activity and selectivity could be attributed to the involvement of OVs. The increased OVs could provide more active sites for stable reduction intermediates, thereby reducing

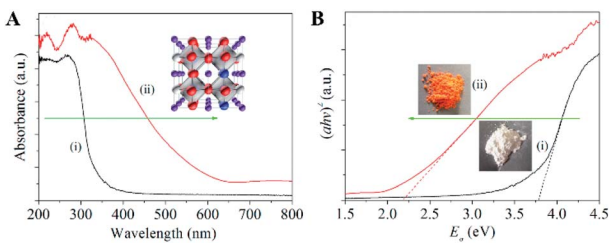

Fig. 8 (A) UV-vis diffuse reflectance spectra of (i) $NaTaO_3$ and (ii) Vo-NaTaON crystals. (B) Band-gap energy of (i) $NaTaO_3$ and (ii) Vo-NaTaON crystals. Reproduced with permission: Copyright 2016 Elsevier Ltd. All rights reserved.[45]

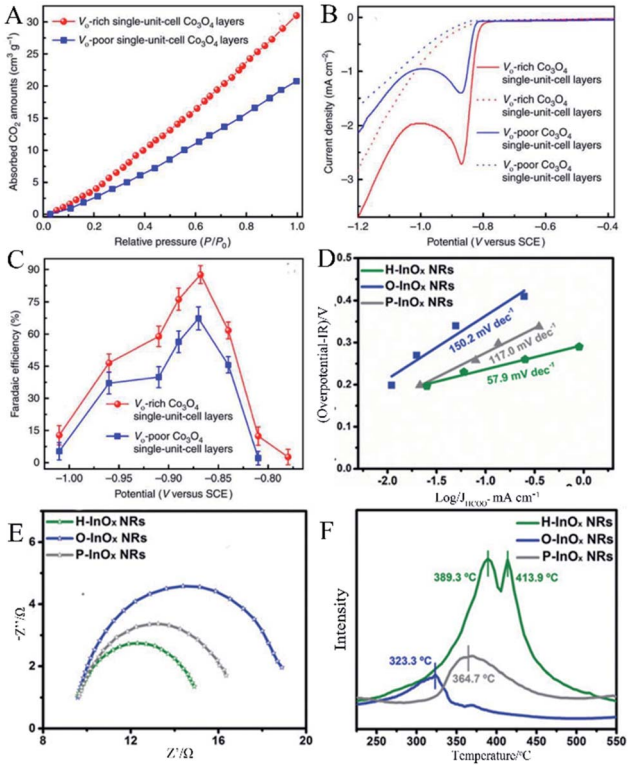

Fig. 9 (A) Linear sweep voltammetric curves in a CO_2-saturated (solid line) and N_2-saturated (dashed line) 0.1 M $KHCO_3$ aqueous solution, (B) faradaic efficiencies of formate at different applied potentials, (C) CO_2 adsorption isotherms. Reproduced with permission: Copyright 2020 Springer Nature Limited.[46] (D) Tafel plots of $HCOO^-$, (E) Nyquist plots, (F) CO_2-TPD profiles of the P-InO_x NRs, O-InO_x NRs, and H-InO_x NRs.Reproduced with permission: Copyright 2019 Wiley-VCH Verlag GmbH & Co. KGaA, Weinheim.[47]

the activation energy barrier. In the measurement of CO_2 adsorption, the result in Fig. 9C exhibits that the OVs-rich Co_3O_4 single-unit-cell layers had a higher CO_2 adsorption capacity than that of the OVs-poor Co_3O_4 single-unit-cell layers, indicating that a higher OVs concentration contributed to an increase in CO_2 adsorption.

Zhang *et al.*[47] prepared a series of OV-engineered InO_x nanoribbons to enhance the absorption and activation of CO_2, thereby improving the CO_2 electrical reduction ability. Fig. 9D shows the current density of $HCOO^-$ under various overpotentials and the corresponding fitted Tafel slopes. The Tafel slopes of O-InO_x NR, P-InO_x NR, and H-InO_x NR are 150.2, 117.0, and 57.9 mV dec^{-1}, respectively, in which the Tafel slope of H-InO_x NR was the lowest, demonstrating that the adsorption capacity was enhanced due to the presence of OVs. Nyquist plots were used to evaluate the interface charge transfer resistance, as shown in Fig. 9E. Obviously, the charge transfer resistance of the H-InO_x NRs was the smallest, which means fastest CO_2 adsorption, charge transfer, and intermediate formation processes. This is because the introduction of OVs enhanced the selectivity of CO_2 reduction. To further investigate the effect of the presence of OVs on the adsorption capacity of CO_2 molecules, temperature programmed CO_2 desorption (CO_2-

TPD) was carried out and is shown in Fig. 9F. The CO chemical desorption temperature is arranged in the order O-InO_x NRs (323.3 °C) < P-InO_x NRs (364.7 °C) < H-InO_x NRs (389.3 °C and 413.9 °C), indicating the most capable adsorption of CO_2 by H-InO_x NRs. The enhanced peaks of the H-InO_x NRs at higher temperature further showed that the introduction of the OVs could significantly promote the chemisorption capacity of CO_2, leading to high activity for CO_2 reduction.

5. Conclusions

Climate change caused by excessive CO_2 emission has received global attention. Using photoreduction and electric reduction methods, CO_2 can be converted into valuable fuel substances such as CO and CH_4. However, limited by the lack of activity and selectivity of the original catalytic material, CO_2 reduction still cannot be put into practical use. Therefore, a variety of methods for introducing oxygen defects are listed, including efficient techniques such as heat treatment, doping, and illumination. Various characterization methods of oxygen defects are also summarized. The key point is to perform a qualitative analysis of the oxygen defects contained in the material by combining these characterization methods and to compare the content of oxygen defects generated. Oxygen defects mainly play a role in increasing the light absorption of the catalyst, providing the adsorption and activation sites, effectively improving the stability of the reaction intermediate during the CO_2 reduction process, and maintaining great influence on the catalyst activity and selectivity. A deeper understanding of the structural modification produced by these materials themselves will further promote the industrialization of CO_2 emission reduction, enabling it to be put into practical use on a large scale, and effectively improving actual energy problems and excessive CO_2 emissions.

Conflicts of interest

There are no conflicts to declare.

Acknowledgements

This work was supported by the State Key Research Development Program of China (no. 2016YFA0204200). Project supported by Shanghai Municipal Science and Technology Major Project (grant no. 2018SHZDZX03) and the Program of Introducing Talents of Discipline to Universities (B16017). National Natural Science Foundation of China (no. 21822603, 21811540394, 21677048, 21773062 and 21577036), and the Fundamental Research Funds for the Central Universities.

References

1 Y. Fu, D. Sun, Y. Chen, R. Huang, Z. Ding, X. Fu and Z. Li, *Angew. Chem., Int. Ed.*, 2012, **51**, 3364–3367.
2 K. Caldeira and M. E. Wickett, *Nature*, 2003, **425**, 365.
3 J. Yu, L.-H. Xie, J.-R. Li, Y. Ma, J. M. Seminario and P. B. Balbuena, *Chem. Rev.*, 2017, **117**, 9674–9754.
4 D. W. Keith, G. Holmes, D. S. Angelo and K. Heidel, *Joule*, 2018, **2**, 1573–1594.
5 Z. W. Seh, J. Kibsgaard, C. F. Dickens, I. Chorkendorff, J. K. Nørskov and T. F. Jaramillo, *Science*, 2017, **355**, eaad4998.
6 Y. Pu, Y. Luo, X. Wei, J. Sun, L. Li, W. Zou and L. Dong, *Appl. Catal., B*, 2019, **254**, 580–586.
7 H.-P. Liang, A. Acharjya, D. A. Anito, S. Vogl, T.-X. Wang, A. Thomas and B.-H. Han, *ACS Catal.*, 2019, **9**, 3959–3968.
8 S. Gao, B. Gu, X. Jiao, Y. Sun, X. Zu, F. Yang, W. Zhu, C. Wang, Z. Feng and B. J. Ye, *J. Am. Chem. Soc.*, 2017, **139**, 3438–3445.
9 X. Jiao, Z. Chen, X. Li, Y. Sun, S. Gao, W. Yan, C. Wang, Q. Zhang, Y. Lin and Y. J. Luo, *J. Am. Chem. Soc.*, 2017, **139**, 7586–7594.
10 Y. Ji and Y. Luo, *J. Am. Chem. Soc.*, 2016, **138**, 15896–15902.
11 N. Guo, H. Xue, A. Bao, Z. Wang, J. Sun, T. Song, X. Ge, W. Zhang, K. Huang and F. He, *Angew. Chem., Int. Ed.*, 2020, **59**, 13778–13784.
12 M. Lu, J. Liu, Q. Li, M. Zhang, M. Liu, J. L. Wang, D. Q. Yuan and Y. Q. Lan, *Angew. Chem., Int. Ed.*, 2019, **131**, 12522–12527.
13 P. Wu, Y. Li, J.-J. Zheng, N. Hosono, K.-I. Otake, J. Wang, Y. Liu, L. Xia, M. Jiang and S. Sakaki, *Nat. Commun.*, 2019, **10**, 1–8.
14 T. Fogeron, P. Retailleau, L. M. Chamoreau, Y. Li and M. Fontecave, *Angew. Chem., Int. Ed.*, 2018, **57**, 17033–17037.
15 A. Fujishima and K. Honda, *Nature*, 1972, **238**, 37–38.
16 X. Chang, T. Wang and J. Gong, *Energy Environ. Sci.*, 2016, **9**, 2177–2196.
17 L. Wang, W. Chen, D. Zhang, Y. Du, R. Amal, S. Qiao, J. Wu and Z. Yin, *Chem. Soc. Rev.*, 2019, **48**, 5310–5349.
18 X. Sun, L. Lu, Q. Zhu, C. Wu, D. Yang, C. Chen and B. Han, *Angew. Chem., Int. Ed.*, 2018, **57**, 2427–2431.
19 W. Zhu, L. Zhang, S. Liu, A. Li, X. Yuan, C. Hu, G. Zhang, W. Deng, K. Zang and J. Luo, *Angew. Chem., Int. Ed.*, 2020, **59**, 12664–12668.
20 F. Y. Gao, S. J. Hu, X. L. Zhang, Y. R. Zheng, H. J. Wang, Z. Z. Niu, P. P. Yang, R. C. Bao, T. Ma and Z. Dang, *Angew. Chem., Int. Ed.*, 2020, **132**, 8784–8790.
21 J. Di, C. Zhu, M. Ji, M. Duan, R. Long, C. Yan, K. Gu, J. Xiong, Y. She and J. Xia, *Angew. Chem., Int. Ed.*, 2018, **57**, 14847–14851.
22 Z. Geng, X. Kong, W. Chen, H. Su, Y. Liu, F. Cai, G. Wang and J. Zeng, *Angew. Chem., Int. Ed.*, 2018, **57**, 6054–6059.
23 X. Jin, C. Lv, X. Zhou, L. Ye, H. Xie, Y. Liu, H. Su, B. Zhang and G. Chen, *ChemSusChem*, 2019, **12**, 2740–2747.
24 L. Lu, B. Wang, S. Wang, Z. Shi, S. Yan and Z. Zou, *Adv. Funct. Mater.*, 2017, **27**, 1702447.
25 Y. Tong, H. Guo, D. Liu, X. Yan, P. Su, J. Liang, S. Zhou, J. Liu, G. Q. Lu and S. X. Dou, *Angew. Chem., Int. Ed.*, 2020, **59**, 7356–7361.
26 M. Vasilopoulou, A. M. Douvas, D. G. Georgiadou, L. C. Palilis, S. Kennou, L. Sygellou, A. Soultati, I. Kostis, G. Papadimitropoulos and D. Davazoglou, *J. Am. Chem. Soc.*, 2012, **134**, 16178–16187.

27 F. C. Calaza, Y. Xu, D. R. Mullins and S. H. Overbury, *J. Am. Chem. Soc.*, 2012, **134**, 18034–18045.
28 T. W. Kim, Y. Ping, G. A. Galli and K.-S. Choi, *Nat. Commun.*, 2015, **6**, 1–10.
29 Y. Wang, B. Wang, Y. Xu, M. Fang, Z. Wu, W. Zhu, J. Hong and C. Li, *J. Chin. Chem. Soc.*, 2017, **64**, 188–194.
30 W. Zhang, L. Cai, S. Cao, L. Qiao, Y. Zeng, Z. Zhu, Z. Lv, H. Xia, L. Zhong and H. Zhang, *Adv. Mater.*, 2019, **31**, 1906156.
31 H. Liu, H. Ma, X. Li, W. Li, M. Wu and X. Bao, *Chemosphere*, 2003, **50**, 39–46.
32 M. Kim, B. Lee, H. Ju, J. Y. Kim, J. Kim and S. W. Lee, *Adv. Mater.*, 2019, **31**, 1903316.
33 K. Liu, W. Zhang, F. Lei, L. Liang, B. Gu, Y. Sun, B. Ye, W. Ni and Y. Xie, *Nano Energy*, 2016, **30**, 810–817.
34 K. Zhang, G. Zhang, J. Qu and H. Liu, *Small*, 2018, **14**, 1802760.
35 Y. Zhao, Y. Zhao, R. Shi, B. Wang, G. I. Waterhouse, L. Z. Wu, C. H. Tung and T. Zhang, *Adv. Mater.*, 2019, **31**, 1806482.
36 S. Feng, T. Wang, B. Liu, C. Hu, L. Li, Z. J. Zhao and J. Gong, *Angew. Chem., Int. Ed.*, 2020, **59**, 2044–2048.
37 Y. Qi, L. Song, S. Ouyang, X. Liang, S. Ning, Q. Zhang and J. Ye, *Adv. Mater.*, 2020, **32**, 1903915.
38 L. Zhang, W. Wang, D. Jiang, E. Gao and S. Sun, *Nano Res.*, 2015, **8**, 821–831.
39 D. Liu, C. Wang, Y. Yu, B.-H. Zhao, W. Wang, Y. Du and B. Zhang, *Chem*, 2019, **5**, 376–389.
40 G. Ahmed, F. Raziq, M. Hanif, J. Khan, K. S. Munawar, M. Wu, X. Cao and Z. Liu, *Sci. Rep.*, 2019, **9**, 1–8.
41 K. Karmakar, A. Sarkar, K. Mandal and G. G. Khan, *ChemElectroChem*, 2018, **5**, 1147–1152.
42 J. Wu, X. Li, W. Shi, P. Ling, Y. Sun, X. Jiao, S. Gao, L. Liang, J. Xu and W. Yan, *Angew. Chem., Int. Ed.*, 2018, **130**, 8855–8859.
43 F. Wang, S. He, H. Chen, B. Wang, L. Zheng, M. Wei, D. G. Evans and X. Duan, *J. Am. Chem. Soc.*, 2016, **138**, 6298–6305.
44 H. Yu, J. Li, Y. Zhang, S. Yang, K. Han, F. Dong, T. Ma and H. Huang, *Angew. Chem., Int. Ed.*, 2019, **58**, 3880–3884.
45 J. Hou, S. Cao, Y. Wu, F. Liang, L. Ye, Z. Lin and L. Sun, *Nano Energy*, 2016, **30**, 59–68.
46 S. Gao, Z. Sun, W. Liu, X. Jiao, X. Zu, Q. Hu, Y. Sun, T. Yao, W. Zhang and S. Wei, *Nat. Commun.*, 2017, **8**, 1–9.
47 J. Zhang, R. Yin, Q. Shao, T. Zhu and X. Huang, *Angew. Chem., Int. Ed.*, 2019, **58**, 5609–5613.